ADVANCED HEALTHCARE MATERIALS
www.advhealthmat.de

Cellular Alignment and Matrix Stiffening Induced Changes in Human Induced Pluripotent Stem Cell Derived Cardiomyocytes

*Andrew House, Anjeli Santillan, Evan Correa, Victoria Youssef, and Murat Guvendiren**

Biological processes are inherently dynamic, necessitating biomaterial platforms capable of spatiotemporal control over cellular organization and matrix stiffness for accurate study of tissue development, wound healing, and disease. However, most in vitro platforms remain static. In this study, a dynamic biomaterial platform comprising a stiffening hydrogel is introduced and achieved through a stepwise approach of addition followed by light-mediated crosslinking, integrated with an elastomeric substrate featuring strain-responsive lamellar surface patterns. Employing this platform, the response of human induced pluripotent stem cell-derived cardiomyocytes (hIPSC-CMs) is investigated to dynamic stiffening from healthy to fibrotic tissue stiffness. The results demonstrate that culturing hIPSC-CMs on physiologically relevant healthy stiffness significantly enhances their function, as evidenced by increased sarcomere fraction, wider sarcomere width, significantly higher connexin-43 content, and elevated cell beating frequency compared to cells cultured on fibrotic matrix. Conversely, dynamic matrix stiffening negatively impacts hIPSC-CM function, with earlier stiffening events exerting a more pronounced hindering effect. These findings provide valuable insights into material-based approaches for addressing existing challenges in hIPSC-CM maturation and have broader implications across various tissue models, including muscle, tendon, nerve, and cornea, where both cellular alignment and matrix stiffening play pivotal roles in tissue development and regeneration.

1. Introduction

The native tissue comprises a dynamic extracellular microenvironment (ECM), which presents spatial and temporal cell-instructive cues, including topographical, mechanical, and biochemical signals. Cells sense and react to these cues by regulating functions such as proliferation, spreading, migration, and differentiation.[1] Consequently, there's a growing interest in designing biomaterial platforms that mimic the native ECM to modulate cellular behavior, aiming to create in vitro tissue and disease models.

Given that heart disease is presently the leading cause of mortality worldwide, there has been a notable surge in interest surrounding cardiac tissue. Understanding the intricacies of cardiac tissue function, development, and pathology is crucial for developing effective treatments and preventative measures. In cardiac tissue, a highly organized collagen-based ECM structure ensures the spatial alignment of cardiac cells, facilitating synchronized contractility.[2] However, in diseased hearts, particularly post-myocardial infarction (MI), excessive collagen production leads to scar formation, locally altering cardiac tissue stiffness and organization. This alteration is known to result in progressive fibrosis and ventricular dilatation.[3] Hence, there is significant interest in developing in vitro platforms capable of dynamically controlling matrix stiffness and cellular alignment to study the response of cardiac cells to post-MI cardiac tissue remodeling. Such platforms hold promise for advancing our understanding of cardiac disease mechanisms and for the development of novel therapeutic interventions.

There has been sustained interest in developing dynamic in vitro platforms capable of inducing matrix stiffening to investigate the effects of such stiffening on cellular behavior during tissue fibrosis.[4] These platforms utilize various triggers for matrix stiffening, including light,[5] temperature,[6] pH,[7] or the addition of biomolecules.[8] A recently devised alternative platform facilitates the transfer of cultured cardiac cells from one matrix to another with adjustable stiffness levels, offering a novel approach to studying the impact of altered matrix stiffness.[9] However, none of these platforms currently enable the control of cellular

A. House, M. Guvendiren
Department of Chemical and Materials Engineering
New Jersey Institute of Technology
University Heights
Newark, NJ 07102, USA
E-mail: muratg@njit.edu
A. Santillan, M. Guvendiren
Department of Biomedical Engineering
New Jersey Institute of Technology
University Heights
Newark, NJ 07102, USA
E. Correa, V. Youssef
Federated Department of Biological Sciences
New Jersey Institute of Technology
University Heights
Newark, NJ 07102, USA

The ORCID identification number(s) for the author(s) of this article can be found under https://doi.org/10.1002/adhm.202402228

DOI: 10.1002/adhm.202402228

alignment alongside matrix stiffening, a critical factor for cardiac tissue development and contraction.[10] Topographical patterning has been demonstrated to effectively influence cardiac cell alignment through contact guidance,[11] and platforms combining surface topography with physiological stiffness have shown promise in promoting cardiac cell function.[12] Nonetheless, existing platforms only provide static presentation of surface patterns and matrix stiffness.

Corbin et al. addressed this limitation by incorporating magnetic iron particles into a poly(dimethylsiloxane) (PDMS) elastomer, resulting in a magnetorheological elastomer (MRE) capable of stiffening in the presence of cardiac cells when subjected to a magnetic field.[13] This innovative system was further advanced by integrating elastomer-grafted tissue arrays to simulate cardiac afterload.[14] Zeng et al. took a similar approach by creating topographically patterned MRE substrates to examine the short-term cellular responses to dynamic stiffening in aligned human ventricular cardiac fibroblasts.[15] Despite the applied magnetic field inducing stiffening of the MRE material, stiffness rapidly reverted to its original state upon removal of the magnetic field.[13] Additionally, variations in substrate surface roughness and stiffness arose due to localized differences in magnetic particle density and configuration, as well as the stiffening process itself, potentially impacting cellular behavior and subsequent cellular responses to stiffening.

To address these limitations, we present a novel dynamic biomaterial platform that integrates a stiffening hydrogel system with an elastomeric substrate featuring strain-responsive wrinkling patterns. The stiffening hydrogel offers a tunable initial stiffness akin to healthy cardiac tissue, and undergoes rapid matrix stiffening within seconds upon exposure to light, mimicking the stiffness characteristic of fibrotic tissue. This process allows for precise spatial control and ensures long-term structural stability. Meanwhile, the elastomeric substrate exhibits dynamic, reversible lamellar patterns with customizable sizes and high fidelity. When combined, this dynamic platform enables independent control of cellular alignment and matrix stiffening. As mentioned above, native ECM becomes stiffer due to excessive deposition of collagen fibers. Our stiffening approach does not mimic the change in composition of the matrix but rather mimics the change in stiffness. With our platform, we explore the effects of matrix stiffening on the behavior of human-induced pluripotent stem cell-derived cardiomyocytes (hIPSC-CMs). Although the response of CMs is known to be modulated by the presence of other cells including fibroblasts, this feasibility study is focused on hIPSC-CM monoculture. These cells are a preferred choice for developing patient-specific cardiac models due to their capacity to capture patient-specific genetic information.[16] However, achieving mature cardiomyocytes poses a challenge, as they typically resemble immature fetal cardiomyocytes in terms of morphology, sarcomere length, gap junctions, and conduction velocities.[17] Despite recent advancements in culture platforms aimed at enhancing hIPSC-CM maturation, including electrical and mechanical stimulation,[18] cellular alignment and morphology optimization,[19] stiffness modulation,[20] soluble factors,[21] and prolonged culture durations,[22] the combined effect of cellular alignment and matrix stiffening on hIPSC-CM function remains unexplored. Thus, our dynamic platform provides an ideal model to investigate these phenomena.

In this study, we first focused on developing the dynamic biomaterial platform and then demonstrated its feasibility for micro-tissue formation using hIPSC-CMs, including investigating the effects of patterning and stiffness on hIPSC-CM behavior. Finally, we examined the effects of dynamic stiffening on highly aligned hIPSC-CM micro-tissues. While our study primarily targets cardiac tissue, our platform has broader implications for other tissue models, such as muscle, tendon, nerve, and cornea, where cellular alignment and matrix stiffening are also crucial.

2. Results and Discussion

2.1. Fabrication of the Dynamic Biomaterial Platform

In this study, we introduce a dynamic biomaterial platform comprised of a stiffening hydrogel matrix integrated with an elastomeric substrate featuring strain-responsive lamellar surface patterns (**Figure 1a**). To achieve this, a rectangular-shaped PDMS film (1mm thick) underwent uniaxial stretching, followed by exposure to ultraviolet/ozone (UVO) and functionalization with methacrylate moiety using 3-(trimethoxysilyl)propyl methacrylate (TMS). A droplet of methacrylated alginate (MeAlg) solution (3wt/vol%) containing a crosslinker, dithiothreitol (DTT), was then placed onto the stretched PDMS surface. The resultant MeAlg hydrogel, characterized by uniform stiffness, formed via a Michael-type addition crosslinking reaction between methacrylates (MeAlg) and thiols (DTT), with the methacrylates on PDMS surface ensuring chemical attachment of the hydrogel to the stretched PDMS film. Upon release of the PDMS film, the surface buckled perpendicular to the stretching direction, generating lamellar patterns. Notably, UVO exposure resulted in formation of a stiffer skin layer (≈5 nm) atop the PDMS film,[23] leading to the emergence of lamellar patterns perpendicular to the applied strain upon strain removal due to the modulus mismatch between the skin and bulk.[24]

The equilibrium pattern wavelength (λ) and amplitude (A) could be controlled by the initial applied strain and UVO exposure time.[25] For this study, the UVO exposure time was kept constant (3 h), while the initial applied strain was varied to obtain two sets of lamellar patterns with a fixed λ of ≈60 μm but varying A, with $A \approx 12$ μm for $\epsilon = 0.2$, and $A \approx 5$ μm for $\epsilon = 0.4$.[26]

Upon strain removal, the PDMS film buckled, forming lamellar patterns perpendicular to the stretching direction, with the MeAlg hydrogel layer conforming to the patterned surface (Figure 1b). Additionally, flat hydrogels were fabricated without applying an initial strain (Figure 1c). Hydrogel thickness (≈12–58 μm) was controlled by the MeAlg solution droplet volume (2–10 μL), which did not alter the pattern λ (≈ 60 μm) but led to a decrease in A (9–5 μm) with increasing droplet volume (Figure 1d–f). It has been previously shown that cells cultured on a thin film hydrogel, affixed to a stiffer substrate, perceive the stiffness of the underlying substrate to a depth of ≈4 μm.[27] To mitigate the influence of the PDMS substrate stiffness on cell behavior, the hydrogel film thickness was set to ≈13 μm, necessitating only 2 μL of droplet and minimizing the decrease in pattern A, which significantly impacts cardiac cell alignment.[26] Furthermore, covering the droplet with a glass slide during crosslinking ensured the formation of hydrogels

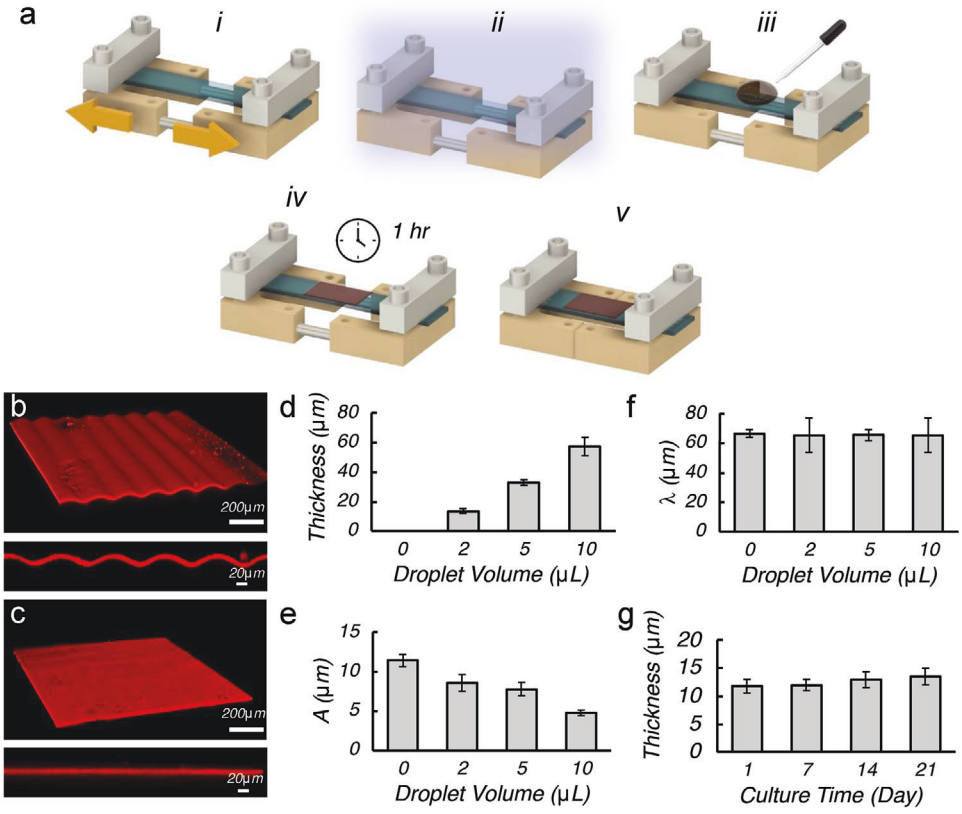

Figure 1. a) Schematic showing fabrication of the dynamic hydrogel platform including (i) stretching of the PDMS film, (ii) UVO exposure, (iii) surface functionalization followed by placing of a droplet of hydrogel solution, (iv) addition-only crosslinking of the hydrogel film, and (v) release of the PDMS film for lamellar pattern formation. b, c) Confocal images showing the hydrogel film (red) attached onto PDMS film including surface (top) and cross-sectional (bottom) views of the patterned (b) and flat (c) hydrogels. Scale bars are 200 and 20 μm. Methacrylated rhodamine (red) was mixed into hydrogel solution to visualize the hydrogel film. d) Film thickness with hydrogel solution droplet volume. e) Pattern amplitude (A) with droplet volume. f) Pattern wavelength (λ) with droplet volume. g) Hydrogel film thickness with culture time. Data are presented as mean ± std for n = 3 samples and 9 total measurements.

with uniform thickness. Importantly, the initial film thickness remained unchanged during long-term culture (Figure 1g).

The initial stiffness of the MeAlg hydrogel was controlled by the consumption of methacrylate groups during the addition-only reaction, which was tuned by the concentration of DTT (**Figure 2a**). For cardiac model studies, the initial stiffness was set to mimic healthy cardiac tissue stiffness (≈10-15 kPa),[28] corresponding to a DTT faction of 0.3, resulting in 14.7 ± 3.4 kPa. This initial hydrogel could be stiffened on demand by UV-induced radical polymerization of the remaining methacrylates when swollen with a photoinitiator (0.05 vol/vol%, Irgacure 2959, I2959), with the final stiffness controlled by UV exposure time (365 nm, 10 mW cm^{-2}) (Figure 2b). Stiffened hydrogels mimicking fibrotic cardiac tissue stiffness (≈55 kPa)[28] were obtained at 2.5 min exposure, resulting in E = 54.7 ± 15 kPa. Rheological analysis of the MeAlg solution confirmed crosslinking via addition-only reaction and subsequent UV-induced radical polymerization (Figure 2c), with stiffening initiating immediately upon UV exposure and modulus equilibrating upon UV light cessation. Finally, hydrogel films with healthy or fibrotic stiffness remained stable under long-term culture conditions (Figure 2d), consistent with the non-degradability of the MeAlg hydrogels in vitro when crosslinked.

Our dynamic platform also enabled spatiotemporal control of matrix stiffening, leading to hydrogels with patterned stiffness. During stiffening process, a photomask was employed to spatially regulate UV exposure (**Figure 3a**). Light penetration through the photomask was controlled by transparent regions featuring user-defined shapes and sizes. Introducing methacrylated rhodamine (MeRho, red) into healthy hydrogel prior to UV crosslinking allowed for selective binding to the UV-exposed, stiffened regions (Figure 3b). When employing a circular pattern, AFM revealed a transition in matrix stiffness from ≈15 kPa (outside the pattern) to ≈55 kPa (within the pattern) (Figure 3c), thereby confirming the spatial control of matrix stiffening.

2.2. Human IPSC-CM Response to Lamellar Patterns and Matrix Stiffness

2.2.1. Cellular Alignment and Cell Shape

We cultured the hIPSC-CMs on our biomaterial platform for up to 21 days (**Figure 4**; Figure S1, Supporting Information) to investigate the effect of lamellar patterns and matrix stiffness on nuclear alignment (**Figure 5a**) as well as cell area and aspect

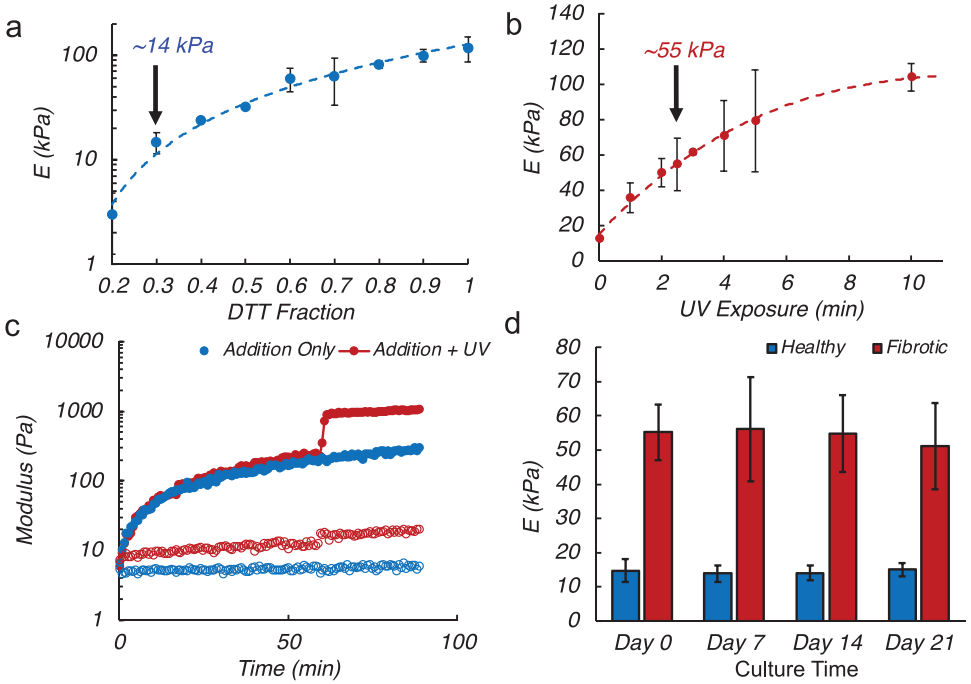

Figure 2. a) MeAlg hydrogel film stiffness (Young's modulus, *E*) for addition-only reaction with varying DTT concentration (at pH 10). b) Stiffness for stiffened MeAlg hydrogel, addition reaction ($E \approx 14$ kPa) followed by UV-induced radical polymerization, with varying UV exposure time. c) Rheology showing hydrogel formation for addition-only reaction (healthy, blue) and stiffened hydrogel, addition reaction followed by UV induced radical polymerization (fibrotic, red). Elastic modulus (G') and viscous modulus (G'') are indicated by solid and open labels, respectively. (d) Stiffness for addition-only (healthy) and for stiffened (fibrotic) hydrogels with culture time. Data for stiffness are presented mean ± std (> 10 random measurements for each sample, n = 3). Day 0 refers to as prepared sample.

ratio (*AR*) (Figure 5b). When hIPSC-CMs were cultured on patterned hydrogels, they exhibited a preference for alignment in the direction of the patterns, whereas on flat hydrogels, they displayed random orientation (Figure 4). We determined the average percentages of cells preferentially aligned with the lamellar patterns by considering cells with nuclei orientation angles within ±20° of the pattern orientation (Figure 5a,c). For cells cultured on healthy stiffness, ≈26% of the cell population on flat hydrogels displayed alignment, whereas on patterned hydrogels, nuclear alignment was 57% for $A = 5$ and 87% for $A = 12$. These findings indicate a significant increase in nuclear alignment with increasing *A*, consistent with our previous results from patterned elastomeric substrates.[26] In contrast, for cells cultured on fibrotic stiffness, nuclear alignment remained unchanged on flat hydrogels (random, ≈27%), but significantly decreased on patterned hydrogels (≈60% for $A = 12$). This suggests that hIPSC-CMs exhibit preferential alignment on patterned hydrogels with healthy stiffness, consistent with previous studies.[12a,29]

When considering cell shape (Figure 5d,e), hIPSC-CMs exhibited a more rounded morphology ($AR = 1.7$) and greater spreading (≈3200 μm^2) with a wider distribution of cell area on flat hydrogels with healthy stiffness. In contrast, cells cultured on patterned hydrogels displayed less spreading (≈2600 and 2100 μm^2 for $A = 5$ and 12) with a narrower cell area distribution and significantly higher cell *AR* ($AR = 2.3$ and 3.4 for $A = 5$ and 12). For cells cultured on fibrotic stiffness, the average cell area (≈4500 and 2800 μm^2 for flat and patterned) and cell area distribution were higher on flat hydrogels, with significantly lower *AR* (1.6 and 2.2 for flat and patterned). This higher cell area (indicating grater spreading) observed on fibrotic stiffness as compared to healthy stiffness is typical for cardiac cells cultured on substrates with stiffness much larger than physiologically relevant stiffness.[20,30] Although our study did not show any evidence of this, the increase in cell area may also be due to hypertrophy, which is associated with a reduction in CM maturation.[31] More detailed gene analyses are required to further investigate this phenomenon, which will be the focus of the future studies.

2.2.2. Intracellular Organization of Sarcomeres

Next, we focused on the intracellular organization of sarcomeres by examining confocal images of immunostained hIPSC-CMs against α-actinin, revealing differences in sarcomere fraction, Z-disk spacing and sarcomere width after 21 days of culture (**Figure 6a**). When cultured on healthy stiffness, the average sarcomere fraction (the amount of cell area taken up by the sarcomeres divided by the total area of each cell) was higher for cells on patterned hydrogels (0.77–0.81) compared to flat hydrogels (≈0.66), with a significant increase observed for highly aligned cells ($A = 12$ μm) (Figure 6b). Similarly, on fibrotic stiffness, the average sarcomere fraction was higher on patterned substrates as compared to flat substrates. However, for highly aligned hIPSC-CMs, the sarcomere fraction was significantly lower for

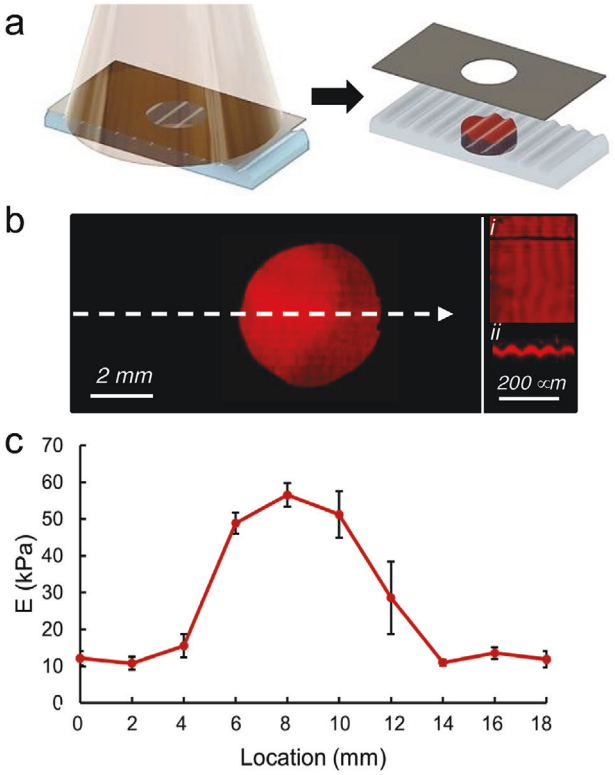

Figure 3. a) Schematic showing spatial control of in situ stiffening by using a photomask. b) Confocal (stitched) image showing the stiffened region with magnified images showing (i) top and (ii) cross-sectional views of the surface patterns. Scale bars are 2 mm and 200 μm. Methacrylated rhodamine (red) was introduced prior to stiffening to visualize the stiffened region as it covalently bounds to the region exposed to UV light. c) Stiffness of the hydrogel measured by AFM along the dotted line shown in (b). Data are presented as mean ± std (> 10 random measurements for each sample with n = 3 samples).

fibrotic stiffness (0.65±0.08) compared to healthy stiffness (0.81 ± 0.09). This reduction may be attributed to decreased cellular alignment on fibrotic stiffness. Sarcomere expression is known to be influenced by substrate stiffness and cellular alignment,[32] such that increased matrix stiffness leads to reduced sarcomere definition and alignment,[30a,33] and cellular alignment enhances sarcomere expression along with an increase in α-actinin density.[19a,34]

While a noticeable difference in Z-disk spacing was observed between the flat and patterned hydrogels, there was no statistically significant difference between healthy and fibrotic stiffness for aligned hIPSC-CMs (Figure 6c). Sarcomere width increased with pattern amplitude, and hence with cellular alignment (Figure 6d). Additionally, for highly aligned cells (A = 12 μm), fibrotic stiffness led to a statistically lower sarcomere width compared to healthy stiffness. This could be attributed to decreased cellular alignment and AR for hIPSC-CMs on fibrotic hydrogels, which have been reported to lead to a lower sarcomere width in the literature.[35] For instance, cellular forces are significantly elevated on physiologically relevant stiffness (≈10 kPa),[30a,36] which are correlated with increased sarcomere lengths and Z-disk spacings.[37]

2.2.3. Cell-Cell Interactions

The presence of gap junctions is crucial for the depolarization of heart muscle and the propagation of the action potentials between cardiac cells.[12b] In this study, we examined the effects of matrix stiffness and cellular alignment on gap junctions through the localization and expression of connexin-43 (Cx43) after 21 days of culture (**Figure 7**). Cx43 expression here refers to relative amount of Cx43 (Figure 7e), based on a semi-quantitative immunostaining analysis rather than direct quantitative methods. Immunostaining for Cx43 revealed abundant localization at the cell-cell contact regions along the cell membrane, with significantly higher expression observed for aligned hIPSC-CMs on patterned hydrogels. The gap junctions appeared with the substrate patterns. It is well-established that myocytes communicate more effectively when aligned compared to randomly oriented cells.[35b,38] Interestingly, Cx43 expression was significantly higher in aligned hIPSC-CMs than in randomly oriented cells, under both healthy and fibrotic stiffness conditions. However, in highly aligned cells, no significant differences in Cx43 expression were observed. These findings are consistent with existing literature. For instance, Cx43 expression remained constant for CMs cultured on PDMS substrates with varying stiffness (≈2–10 kPa), yet significant changes were observed when comparing these cells with CMs cultured on much stiffer glass slides.[20] It should be noted that our approach has limitations, as immunostaining is not a quantitative method for determining Cx43 content, and cytoplasmic and perinuclear staining could superficially increase the calculated Cx43 content. Future studies will include protein analysis (e.g., Wester blotting) to address these limitations.

2.2.4. Cell Beating and Calcium Handling

Intracellular sarcomere organization and cell-cell interactions via gap junctions play pivotal roles in influencing cardiac contractility, synchronous cell beating, and calcium (Ca^{2+}) handling of CMs. In our study, we initially investigated the evolution of synchronous beating in hIPSC-CMs by measuring beating frequency (BF, beats per minute, BPM) over time (**Figure 8A**; Figure S2, Supporting Information). Freshly thawed hIPSC-CMs were cultured on flat or patterned hydrogels with healthy and fibrotic stiffness for 28 days, with measurements beginning after 1 week of culture to allow for the recovery of hIPSC-CMs from cryopreservation.[39] The BF of hIPSC-CMs showed dependence on culture time, with the evolution of BF (Figure 8a) and equilibrium BF (at 28 days, Figure 8b) influenced by the matrix stiffness and cellular alignment. Specifically, BF increased significantly with culture time, reaching an equilibrium BF where no statistically significant differences were observed among BF values between subsequent days. This could be attributed to time-dependent changes in intercellular organization of hIPSC-CMs and the establishment of cell-cell interactions (Figure S3, Supporting Information).[40] For randomly oriented hIPSC-CMs on flat hydrogels, BF reached equilibrium ≈20 days, independent of hydrogel stiffness. In contrast, for aligned hIPSC-CMs on patterned hydrogels, the equilibrium time was delayed to ≈21-22 days, possibly due to additional time needed for cells to adjust

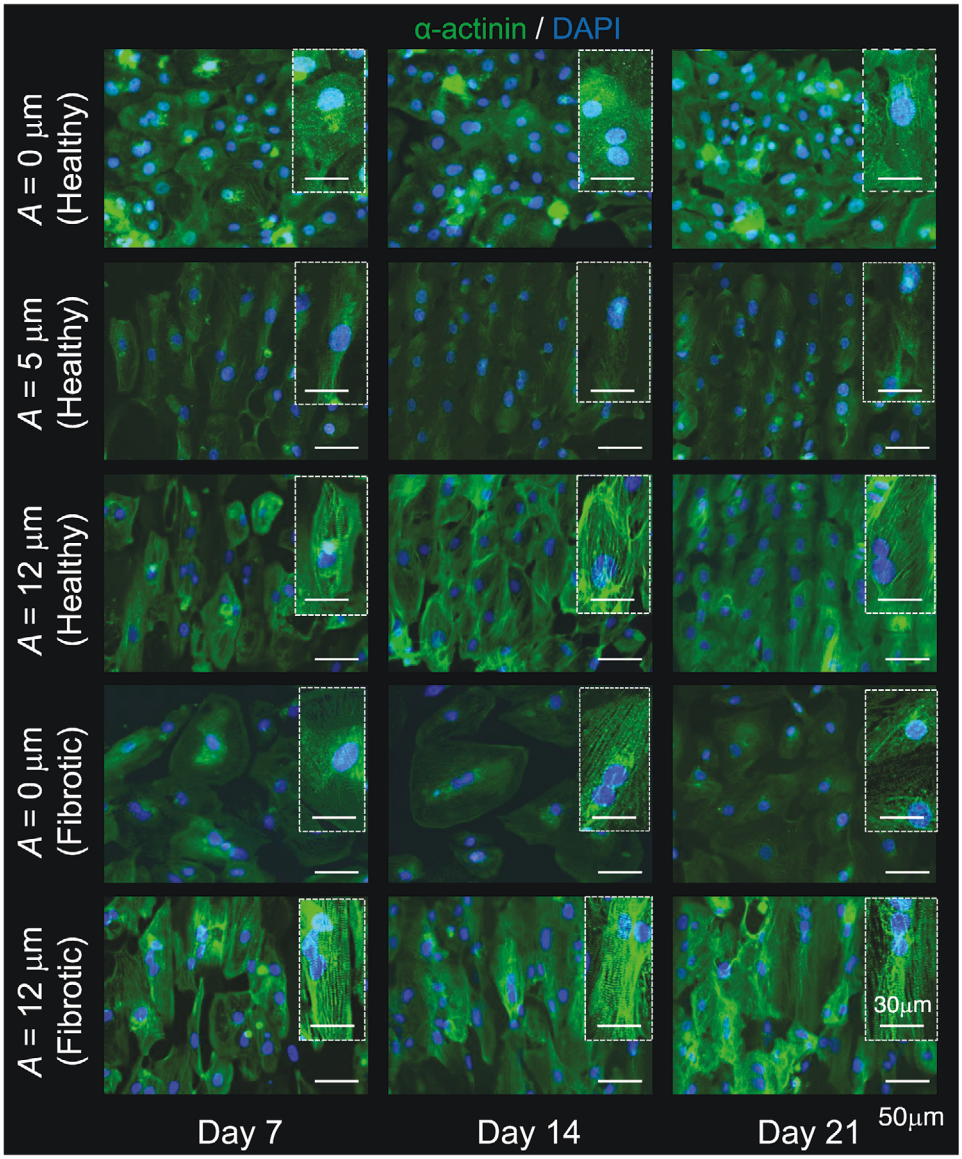

Figure 4. Fluorescent microscope images of hIPSC-CMs (α-actinin (green) and nuclei (DAPI, blue)) cultured on flat or patterned hydrogel platform with healthy or fibrotic stiffness at culture days 7, 14 and 21. Scale bars are 50 μm.

their cell area and AR to conform with surface patterns during cellular alignment. Notably, the equilibrium BF for aligned cells on the patterned hydrogels was significantly higher than that of randomly aligned cells (Figure 8b).

On healthy substrates, BF significantly increased with increasing cellular alignment (or pattern amplitude) such that BF was ≈25, 47, and 54 BPM for nuclear alignment of ≈26% ($A = 0$, flat), 57% ($A = 5$) and 87% ($A = 12$). Although a similar trend was observed on fibrotic stiffness (≈24 BPM for $A = 0$ and ≈39 BPM for $A = 12$), the BF of aligned hIPSC-CMs was significantly higher on healthy stiffness (Figure 8b). Next, we investigated the calcium handling dynamics of hIPSC-CMs by measuring the calcium flux (Figure 8c) using fluorescent microscopy of a cell-permeable Ca^{2+} indicator (Fluo-4 AM). Our results indicated a slight decrease in 50% decay (T50) and a significant decrease in 90% (T90) for hIPSC-CMs cultured on patterned hydrogels as compared to flat hydrogels (Figure 8d), attributable to cellular alignment. These observations align with the trends observed for BF, indicating that cellular alignment led to an increase in BF along with faster Ca^{2+} transient decay. We note that BF alone is not a highly informative metric of cardiomyocyte phenotype; rather, it is used here as a relative metric to compare cellular behavior on different substrates. Overall, our results clearly demonstrate that synchronous cell beating and Ca^{2+} handling were significantly enhanced in highly aligned hIPSC-CMs cultured on substrates with healthy stiffness. These findings are consistent with the previous reports that show cellular alignment and physiologically relevant stiffness enhance electrophysiology of CMs.[20,41] The Ca^{2+} handling metrics are frequency dependent and could be affected by the changes in BF due to substrates conditions. These metrics

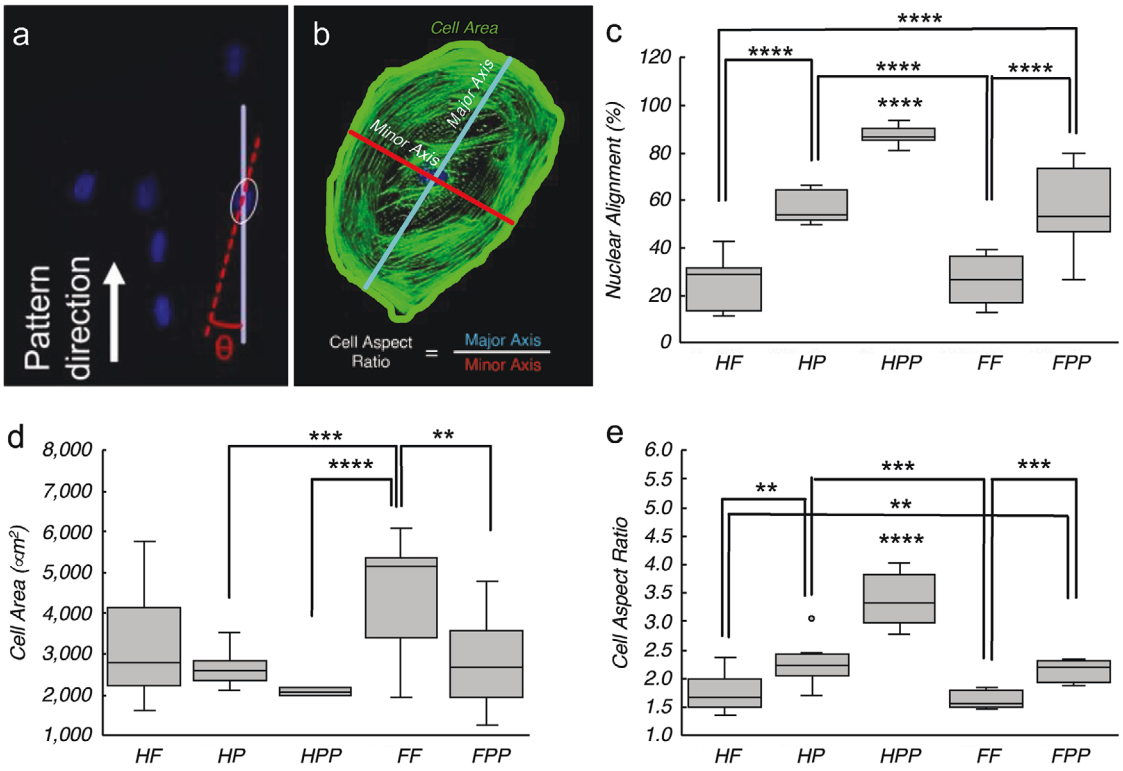

Figure 5. a, b) Representative fluorescent microscopy images of (a) cell nuclei and (b) cell surface area used to measure nuclear alignment, cell area, and cell aspect ratio. The hIPSC-CMs were cultured for 21 days on healthy flat (HF) and patterned (HP with pattern A = 5 μm and HPP with pattern A = 12 μm), and fibrotic flat (FF) and patterned (FPP, A = 12 μm) hydrogels. c) Nuclear alignment for hIPSC-CMs. **** $p < 0.0001$ for HPP vs all groups, for HP vs HF and FF, and for FPP vs HF and FF (n = 135 cells from 3 different batches). d) Cell area for hIPSC-CMs. **** $p < 0.0001$ for HPP vs FF, *** $p < 0.005$ for HP vs FF, ** $p < 0.05$ for FPP vs FF (n = 135 cells from 3 different batches). e) Cell aspect ratio for hIPSC-CMs. **** $p < 0.0001$ for HPP vs all groups, *** $p < 0.005$ for FF vs FPP and HP, ** $p < 0.05$ for HF vs FPP and HP (n = 135 cells from 3 different batches).

could be studied in response to external pacing to decouple the effects of BF, which will be one focus of our future studies.

2.3. The hIPSC-CM Response to Temporal Matrix Stiffening

To investigate the cellular response to matrix stiffening, we employed our dynamic stiffening hydrogel platform with wrinkling patterns, transitioning matrix stiffness from ≈15 kPa (healthy, addition-only) to ≈55 kPa (fibrotic, stiffened) as a model system. In situ matrix stiffening studies involved culturing hIPSC-CMs on healthy patterned (A = 12 μm) matrix for 28 days, during which the hydrogel was stiffened at different times – day 14 (dynamic, Dyn D14) and day 21 (Dyn D21). Stiffening involved introducing a solution of the I2959 photoinitiator in media for 30 min followed by UV light exposure for 2.5 min to stiffen the matrix to fibrotic stiffness in the presence of cells. Control groups included hIPSC-CMs cultured on static healthy and static fibrotic patterned matrices. To assess the effects of experimental parameters during stiffening process (I2959 and UV exposure as well as their combination), a detailed viability study was performed, including mitochondrial activity and membrane permeability (Figure S4, Supporting Information). I2959 incubation followed with 10 min of UV exposure was used as a positive control for damage. No detrimental effects on hIPSC-CMs behaviour were observed, providing evidence of negligible damage to the cells during the stiffening process.

When cultured on static matrices for 28 days, hIPSC-CMs on healthy matrix exhibited high alignment in the direction of patterns (≈90%), statistically larger cell aspect ratio (≈3.5), relatively higher sarcomere fraction (≈0.8), wider sarcomere width (≈6.5 μm), and significantly higher Cx43 expression (≈9%) compared to cells on fibrotic matrix (alignment = ≈66%, aspect ratio = ≈2.7, sarcomere fraction = ≈0.7, sarcomere width = ≈5, and Cx43 expression = ≈7%). The hIPSC-CMs on healthy matrix reached an equilibrium BF of ≈56 BPM compared to ≈35 BPM on fibrotic matrix. When hIPSC-CMs were cultured on healthy matrix for 21 days followed by stiffened fibrotic matrix for 14 days (Dyn D21), no statistical differences were observed in cell function, including nuclear alignment, sarcomere width, Z-disk spacing, sarcomere fraction and Cx43 expression, except for a decrease in cell AR, compared to cells on healthy static matrix (**Figure** 9a–f). For hIPSC-CMs cultured only 14 days on healthy matrix followed by 21 days on stiffened matrix (Dyn D14), cellular function was similar to that of cells cultured on static fibrotic matrix for 28 days. The evolution of BF for hIPSC-CMs on Dyn D14 and Dyn D21 was similar to that of cells cultured on static healthy and fibrotic stiffness, respectively (Figure 9g). However, the equilibrium BF of cells significantly differed for each condition. Notably, on Dyn D14 matrix, the equilibrium BF (≈39 BPM) was closer to that of

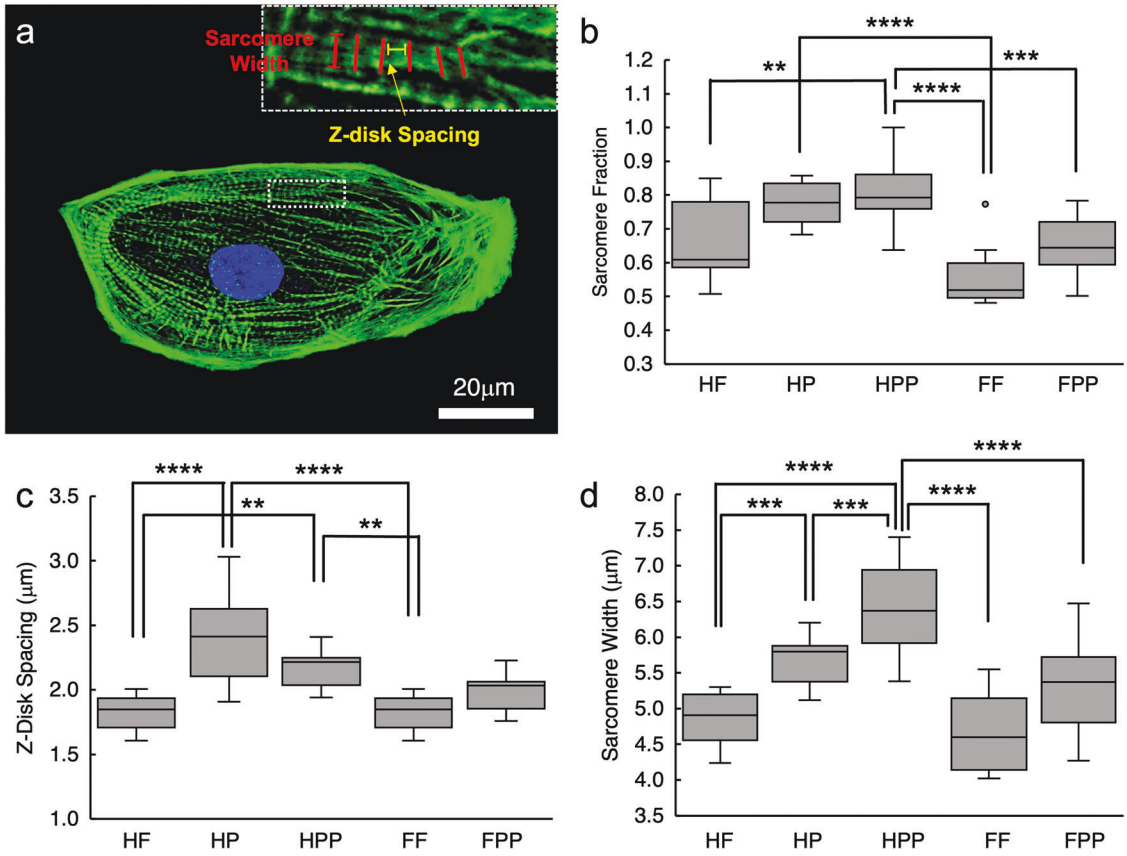

Figure 6. a) Representative fluorescent microscopy image of an hIPSC-CM stained for α-actinin (green) and nuclei (blue). Inset shows a zoomed in region (white dotted box) to visualize sarcomere width and Z-disk spacing. The hIPSC-CMs were cultured for 21 days on healthy flat (HF) and patterned (HP with pattern $A = 5$ μm and HPP with pattern $A = 12$ μm), and fibrotic flat (FF) and patterned (FPP, A = 12 μm) hydrogels. b) Sarcomere fraction, the amount of cell area taken up by the sarcomeres divided by the total area of each cell, for hIPSC-CMs. **** $p < 0.0001$ for HP vs FF and for HPP vs FF, *** $p < 0.005$ for HPP and FPP, ** $p < 0.05$ for HPP vs HF (n = 135 cells from 3 different batches). c) Z-disk spacing for hIPSC-CMs. **** $p < 0.0001$ for HP vs HF and FF, ** $p < 0.01$ for HPP vs HF and FF (n = 135 cells from 3 different batches). d) Sarcomere width for hIPSC-CMs. **** $p < 0.0001$ for HPP vs HF, FF and FPP, *** $p < 0.005$ for HP vs HF and HPP (n = 135 cells from 3 different batches).

cells on fibrotic matrix (≈35 BPM), whereas cells on Dyn D21 matrix, the equilibrium BF (≈52 BMP) was closer to that of cells on healthy matrix (≈55 BMP) (Figure 9h). These results underscore that matrix stiffening decreased hIPSC-CM function, with the extent of this decrease being more pronounced for stiffening at earlier culture times. The current study focused on dynamic matrix stiffening on highly aligned hIPSC-CMs on patterned hydrogels with $A = 12$ μm, while not considering the effect of pattern amplitude (or the degree of cellular alignment) on hIPSC-CMs' response to matrix stiffening. Despite recent studies indicating the effect of change in matrix stiffness on CM function[14,42] and cardiac fibroblast activation,[6d] we believe that our results are significant as no previous studies have been reported on the effects of matrix stiffening on the function of highly aligned hIPSC-CMs during long term culture.

3. Conclusion

In summary, we introduced a novel dynamic biomaterial platform that precisely controls cellular alignment and temporal matrix stiffening, mimicking the dynamic processes observed in biological systems such as tissue development and disease progression. By employing lamellar surface patterns and a sequential crosslinking process, our platform allows user-controlled cellular alignment and rapid, well-defined matrix stiffening with long-term stability. This study specifically investigated the behavior of human induced pluripotent stem cell-derived cardiomyocytes (hIPSC-CMs) in this dynamic microenvironment, a notable shift from conventional static tissue culture platforms. We examined how hIPSC-CMs respond to temporal changes in matrix stiffness, simulating conditions akin to tissue maturation.

Our findings demonstrate that while cellular alignment and physiologically relevant matrix stiffness enhance hIPSC-CM function, matrix stiffening negatively affects their performance. Notably, early stiffening events resulted in reduced cellular alignment, increased cell area, and diminished sarcomere length, Cx43 expression, and beat frequency, emphasizing the detrimental effects of premature stiffening.

We acknowledge certain limitations in our study, particularly the need for more direct quantitative methods to assess hIPSC-CM phenotype and maturation, as well as gap junction functionality. These will be the focus of future studies. Additionally, incorporating cardiac fibroblasts could significantly enhance our in vitro model, as fibroblasts play a crucial role in cardiac fibrosis.

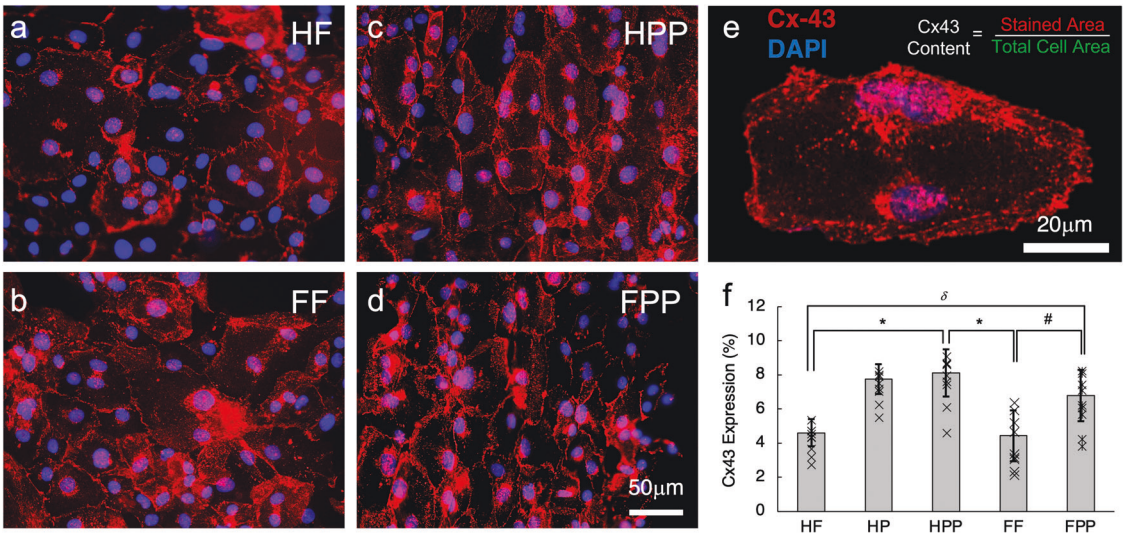

Figure 7. a–d) Representative fluorescent microscopy images of hIPSC-CM immunostained for connexin-43 (Cx43, red) and stained for nuclei (blue). Scale bars are 50 μm. The hIPSC-CMs were cultured for 21 days on (a) healthy flat (HF), (b) fibrotic flat (FF), (c) healthy patterned (HPP with pattern $A = 12$ μm), and (d) fibrotic patterned (FPP, $A = 12$ μm) hydrogels. e) A representative zoomed image showing Cx43 distribution on a cell membrane used for quantification of Cx43 content. f) Cx43 expression for hIPSC-CMs cultured on healthy flat (HF) and patterned (HP with pattern $A = 5$ μm and HPP with pattern $A = 12$ μm), and fibrotic flat (FF) and patterned (FPP, A = 12 μm) hydrogels. Data are presented as mean ± std with n = 9 (3 cells for 3 different batches). Statistical significance is indicated: $^{****}p < 0.0001$, $^{***}p < 0.005$, $^{**}p < 0.05$ (n = 9, 3 cells for 3 different batches).

Overall, this work illuminates the intricate relationship between cellular behavior and microenvironmental cues, underscoring the value of dynamic biomaterial platforms for advancing our understanding of tissue development and disease. Future studies using this platform hold potential for uncovering complex mechanisms driving tissue maturation and pathology, potentially leading to innovative therapeutic approaches.

4. Experimental Section

Macromer Synthesis: Methacrylated alginate (MeAlg) was synthesized following previously established methods.[43] Initially, alginic acid sodium salt from brown algae (Sigma–Aldrich) dissolved in Dulbecco's phosphate-buffered saline (DPBS, Sigma-Aldrich) at a concentration of 3 wt/vol%. Methacrylic anhydride (Sigma-Aldrich) was added to the solution (8 vol/vol%) under magnetic stirring for 12 h at 4°C while maintaining the pH between 8 and 9 using 2M NaOH (Sigma-Aldrich). Subsequently, the solution underwent filtration, followed by dialysis for 7 days (Spectra/Por dialysis membrane, 6–8 kDa molecular weight cutoff, Fischer Scientific). After dialysis, the solution was frozen at -80 °C, and lyophilized (Labconco FreeZone 4.5L, Fisher Scientific).

Fabrication of the Devices: Poly(dimethylsiloxane) (PDMS, Sylgard 184 Elastomer Kit, Dow Corning) sheets (1 mm in thickness) were fabricated using 10 to 1 weight ratio of precursor base to curing agent mixture cured in a 150 mm plastic dish at 60 °C. PDMS sheet was cut into 10×40 mm rectangle films. Each film was clamped onto a custom-made sample holder and stretched uniaxially (20% or 40% of their initial length) or left unstretched (as a control). The top surface of the films was exposed to UV/ozone (UVO, T16×16/OES, UVOCS Inc.) for 3 h, and functionalized with 3-(trimethoxysilyl)propyl methacrylate (TMS) (Sigma-Aldrich) overnight.[44] After the excess TMS was rinsed with ethanol, films were immersed in 70% ethanol solution for 30 min, rinsed with DPBS, and exposed to germicidal lamp inside the biohood for 1 h. MeAlg solution in PBS (3 wt/vol%) containing 0.2 M triethanolamine (at pH 10, Sigma-Aldrich), a photoinitiator (0.05 wt/vol%, I2959, Sigma-Aldrich), and a crosslinker dithiothreitol (DTT, 30 wt/vol% except for variable DTT investigation, Sigma-Aldrich) was sterile filtered and pipetted onto the film surface (2-10 μm droplet). The droplet was covered with a glass slide and incubated for 1 h at room temperature to obtain a crosslinked hydrogel via Michael-type addition reaction. To control stiffness with photopolymerization, films were then exposed to ultraviolet light (10 mW cm^{-2}) for varying exposure times. An oligopeptide, GRGDSPC (GenScript) was added into the macromer solution before DTT addition and reacted for 30 min to couple RGD adhesion moiety into the MeAlg with a final concentration of 1 mM.[5a,43] For imaging purposes, 2μg mL^{-1} methacrylated rhodamine (MeRho, Thermo Fischer Scientific) was added to the macromer solution. After hydrogel formation, the devices were soaked into DPBS to gently lift the glass coverslip. Devices with surface patterns were formed when the stretched films were released gently using a custom-made stretching device. Devices with flat surfaces were formed from unstretched films. Each device was removed from sample holder, cut into 10 × 10 mm square from the center location, placed into a 24-well plate (Costar non-treated, Corning), and fixed with an O-ring (10.2 mm in diameter with 2.6 mm wall size, FETFE Ace O-rings, Sigma-Aldrich).

Characterization of the Devices: AFM was used to characterize the surface topography and stiffness of the devices. AFM studies were done using a Dimension ICON AFM (Bruker) in air for PDMS films, and in PBS using an immersion chamber for the devices (hydrogels equilibrated and submerged in PBS). Surface topography scans were done using ScanAsyst mode (Bruker) to determine the amplitude and wavelength (peak to peak distance) of the patterns. Stiffness measurements were done using PeakForceQNM mode with an MLCT-Bio probe tip with pyramidal geometry (0.03 N m^{-1}, Bruker) for hydrogels and an RFESP-75 probe tip with rotated (symmetric) geometry (0.30 N m^{-1}, Bruker) for PDMS. Confocal microscopy was used to characterize surface patterns and hydrogel film thickness using hydrogel devices containing MeRho. Measurements were done using ImageJ (NIH).

Cell Culture Studies: The human induced pluripotent stem cell-derived cardiomyocytes (hIPSC-CMs) (iCell Cardiomyocytes 01434, FUJIFILM Cellular Dynamics, Inc.) were used in this study. As-received hIPSC-CM vial (≥1 × 10^6 cells/vial) stored in liquid nitrogen was incubated in a water bath at 37°C for 5 min. The vial was sprayed with 70% ethanol, and cell suspen-

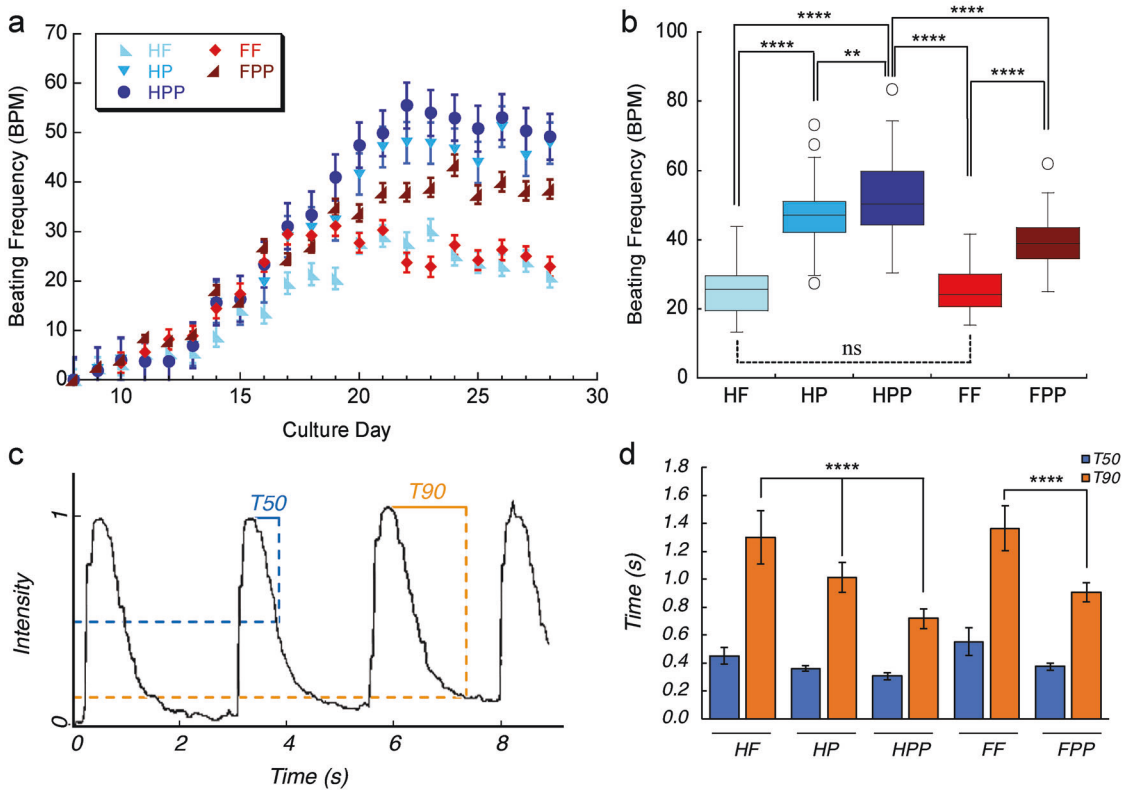

Figure 8. a) Beating frequency of hIPSC-CMs cultured on heathy flat (HF), healthy patterned (HP with A = 5μm and HPP with A = 12μm), fibrotic flat (FF) and fibrotic patterned (FPP with A = 12 μm) hydrogels for 28 days. Data are presented as mean ± se with n = 9 (3 cells for 3 different batches). b) Equilibrium beating frequency of hIPSC-CMs at day 28. Box plots are generated for n ≥ 60 cells from 3 different batches. Statistical significance is indicated: **** $p < 0.0001$, ** $p < 0.05$, ns = no significance. c) Fluorescent intensity of calcium stain from hIPSC-CMs cultured on fibrotic patterned hydrogels depicting the time to 50% (T50, blue) and 90% (T90, orange) decline. d) T50 and T90 values plotted for hIPSC-CMs cultured on HF, HP, HPP, FF, and FPP for 28 days. Data are presented as mean ± std with n = 9 (3 cells for 3 different batches) and statistical significance is indicated: **** $p <$ 0.0001.

sion was pipetted into a 50 mL centrifuge tube inside a biohood. The vial was rinsed with 1 mL of plating medium (iCell Cardiomyocytes Plating Medium, FUJIFILM Cellular Dynamics, Inc. (FCDI)) at room temperature to recover residual cells from the vial, and the solution was pipetted into the centrifuge tube dropwise. To ensure high cell viability, cell suspension was not centrifuged and pipetted directly onto the surface of the devices (≈250 μL cell suspension per device, ≈63×10^3 cells cm^{-2}). Devices were placed into the cell incubator and incubated for 2 days before plating media was replaced with the maintenance media (iCell Cardiomyocytes Maintenance Medium, FUJIFILM Cellular Dynamics, Inc.). Maintenance media was refreshed every other day.

Cell Staining: Cells were fixed in formaldehyde solution (4%) for 15 min and washed in DPBS (2x). For immunostaining, fixed cells were incubated in a blocking buffer (prepared by diluting nonfat dry milk to 3% (w/v) and TritonX-100 to 0.1% (v/v) in DPBS) for 15 min at RT and stained with mouse anti-sarcomeric alpha-actinin (ABCAM) and/or rabbit anti-connexin 43 (Sigma) in blocking buffer (1:100 dilution) at 4°C overnight. Cells were then washed with DPBS (2x) and incubated in corresponding secondary antibodies (1:500 dilution) such as donkey anti-mouse Alexa-Fluor 488 (Invitrogen) and donkey anti-rabbit Alexa-Fluor 647 (Invitrogen) for 30 min at RT, and then stained with DAPI (1:1000 dilution, Sigma-Aldrich) for 5 min at RT. Fluorescent images were acquired using a fluorescent microscope (Olympus IX81) and/or a confocal microscope (Leica TCS SP8).

Quantification of Cell Alignment and Shape: Cell nuclei images were used to quantify the nuclear alignment with respect to the direction of the lamellar patterns. Histograms were generated using an inhouse MATLAB script. Alignment percentage was calculated by dividing the number of nuclei aligned within ±20 degrees of the pattern direction by the total number of cells. Histograms were produced by binning the angles in intervals of 10 degrees. F-actin staining images were used to determine cell area and aspect ratio. ImageJ (NIH) was used for measurements (3 randomly selected locations for n = 3) with total number of measurements ≥ 100 cells.

Imaging-based Quantification of Cell Functionality: Immunostaining images (20x and 40x) were used for sarcomere and connexin-43 analysis. Sarcomere fraction, Z-disk spacing, and sarcomere length were quantified using ImageJ (NIH). Sarcomere fraction was determined by calculating the amount of cell area taken up by the sarcomeres, divided by the total area of each cell. Z-disk spacing was taken as the average distance between each Z-disk. Sarcomere length was taken as the average length of each Z-disk running perpendicularly to the direction of the Z-disk spacing. Analysis of the gap junction was made using an in-house MATLAB script. First, Cx43 immunostaining images were imported into MATLAB. A threshold is used to enhance the contrast of the Cx43 stain and the background, and the image is converted into a binary. The Cx43 ratio is determined by dividing the stained area of the cell with the total cell area. For these measurements, 3 random locations per image for 3 replicates were used (≈15 cells leading to ≈135 total measurements).

Beating Analysis and Calcium Transient Measurements: Live cell imaging was conducted using Olympus IX-81 microscope under 20x

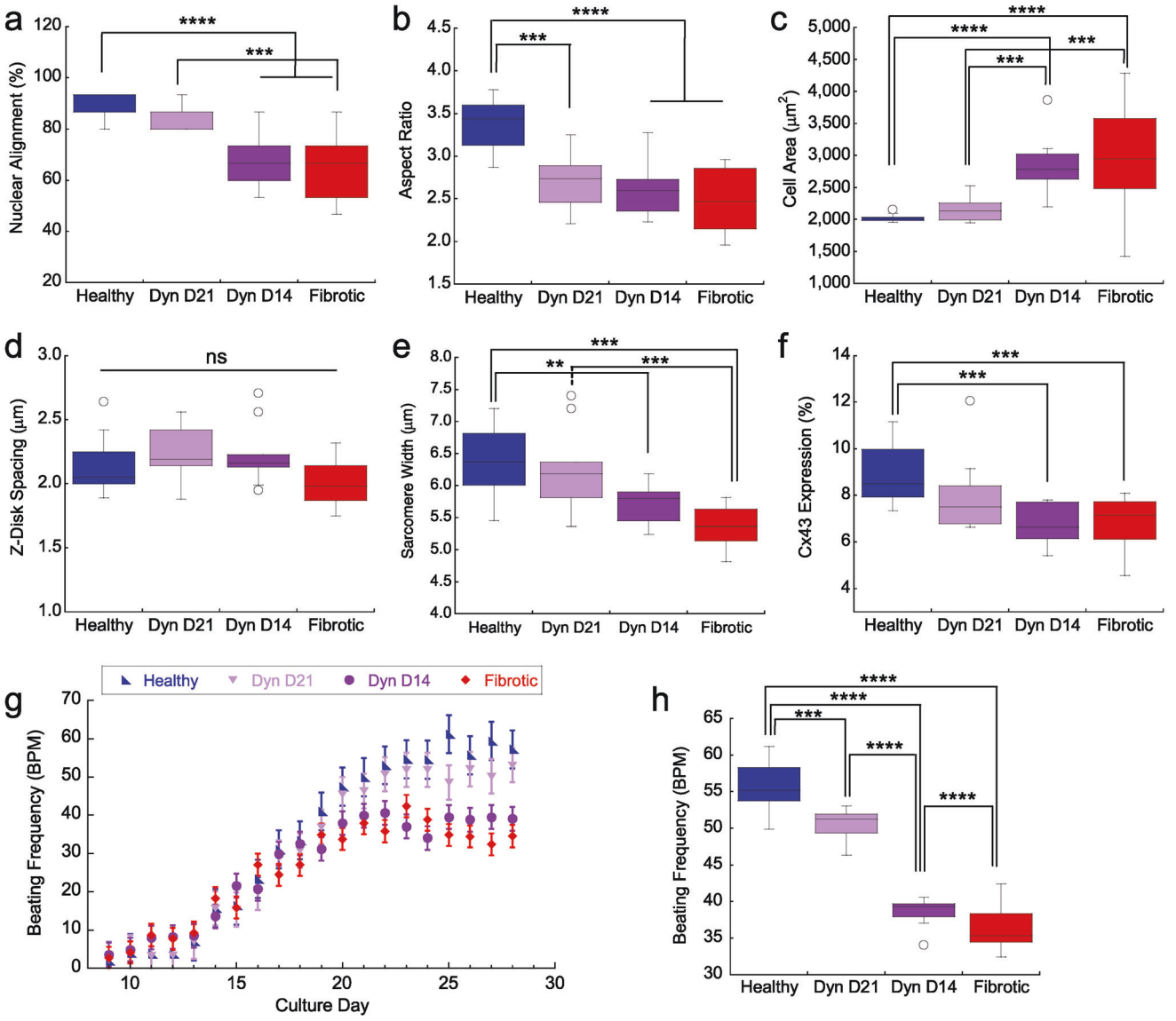

Figure 9. The effect of matrix stiffening from healthy to fibrotic stiffness on hIPSC-CM behavior, including (a) nuclear alignment, (b) cell aspect ratio, (c) cell area, (d) Z-disk spacing, (e) sarcomere length, (f) Cx43 expression, (g) beating frequency and (h) equilibrium beating frequency. The substrate condition is denoted by Dyn D21 and Dyn D14 for dynamic stiffening hydrogels at culture day 21 and 14, respectively, while Healthy and Fibrotic represent static controls. Box plots in (a-f) and (h) are generated for n = 9 at culture day 28, and data in (e) are presented as mean ± se for n = 9. Statistical significance is indicated by asterisks: $^{****}p < 0.0001$, $^{***}p < 0.005$, $^{**}p < 0.05$ (n = 9). Here, n represents total number of cells from 3 different batches.

magnification using the cellSens Dimension software. Cells were observed for a period of 30 s (3 movies per sample for n = 3 replicates) to determine the beating frequency. Calcium activity was recorded with the intracellular calcium-sensitive dye fluo-4 AM (Molecular Probes, Eugene). Briefly, 50 μg of the dye was mixed in 10 μL DMSO, and the mixture diluted in 15 mL of maintenance media. Cells were incubated in this medium for 30 min at 37°C and washed with fresh maintenance media (2x). A custom MATLAB script was used to calculate the normalized times to 50% (T50) and 90% (T90) decay in transients following literature.[35b,45]

Statistical Analysis: The results are reported as mean ± standard deviation. If not stated specifically, three samples per each group was used. Whenever appropriate, comparisons among multiple groups were performed by analysis of variance (ANOVA). A two-tailed Student's t-test was used to discern the statistical difference between two groups, where a probability value (p) of less than 0.05 was considered significant.

Supporting Information

Supporting Information is available from the Wiley Online Library or from the author.

Acknowledgements

This study was supported by an award from the New Jersey Health Foundation and a CAREER award (#2044479) from the National Science Foundation.

Conflict of Interest

The authors declare no conflict of interest.

Data Availability Statement

The data that support the findings of this study are available from the corresponding author upon reasonable request.

Keywords

cardiac tissue models, fibrosis, hydrogels, methacrylated alginate, photopolymerization, wrinkling patterns

Received: July 3, 2024
Revised: October 15, 2024
Published online:

[1] a) D. E. Discher, P. Janmey, Y. L. Wang, *Science* **2005**, *310*, 1139; b) D. E. Discher, D. J. Mooney, P. W. Zandstra, *Science* **2009**, *324*, 1673; c) A. J. Engler, S. Sen, H. L. Sweeney, D. E. Discher, *Cell* **2006**, *126*, 677; d) A. Curtis, C. Wilkinson, *Biomaterials* **1997**, *18*, 1573; e) R. McBeath, D. M. Pirone, C. M. Nelson, K. Bhadriraju, C. S. Chen, *Dev. Cell* **2004**, *6*, 483; f) C. S. Chen, M. Mrksich, S. Huang, G. M. Whitesides, D. E. Ingber, *Science* **1997**, *276*, 1425; g) K. A. Kilian, B. Bugarija, B. T. Lahn, M. Mrksich, *Proc. Natl. Acad. Sci. U S A* **2010**, *107*, 4872.

[2] K. R. Chien, I. J. Domian, K. K. Parker, *Science* **2008**, *322*, 1494.

[3] a) D. D. Streeter, H. M. Spotnitz, D. P. Patel, J. Ross, E. H. Sonnenblick, *Circ. Res.* **1969**, *24*, 339; b) R. C. Gorman, J. H. Gorman, L. M. Parish, M. G. St. John-Sutton, *Ann. Thoracic Surge.* **2004**, *78*, 1507; c) S. Hinderer, K. Schenke-Layland, *Adv. Drug Deliv. Rev.* **2019**, *146*, 77; d) V. Picchio, E. Floris, Y. Derevyanchuk, C. Cozzolino, E. Messina, F. Pagano, I. Chimenti, R. Gaetani, *Int. J. Mol. Sci.* **2022**, *23*, 11642.

[4] a) C. Wang, G. Ramahdita, G. Genin, N. Huebsch, Z. Ma, *Biophys. Rev.* **2023**, *4*, 011314; b) J. A. Burdick, W. L. Murphy, *Nat. Commun.* **2012**, *3*, 1269; c) J. Kim, R. C. Hayward, *Trends Biotechnol.* **2012**, *30*, 426; d) A. House, I. Atalla, E. J. Lee, M. Guvendiren, *Adv Nanobiomed. Res.* **2021**, *1*, 2000022; e) R. A. Marklein, J. A. Burdick, *Adv. Mater.* **2010**, *22*, 175; f) H. Liu, P. Fan, F. Jin, G. Huang, X. Guo, F. Xu, *Front. Bioeng. Biotechnol.* **2022**, *10*, 1042030.

[5] a) M. Guvendiren, J. A. Burdick, *Nat. Commun.* **2012**, *3*, 792; b) A. M. Rosales, S. L. Vega, F. W. DelRio, J. A. Burdick, K. S. Anseth, *Angew. Chem., Int. Ed.* **2017**, *56*, 12132.

[6] a) D. M. Le, K. Kulangara, A. F. Adler, K. W. Leong, V. S. Ashby, *Adv. Mater.* **2011**, *23*, 3278; b) K. A. Davis, K. A. Burke, P. T. Mather, J. H. Henderson, *Biomaterials* **2011**, *32*, 2285; c) S. Hackelbusch, T. Rossow, D. Steinhilber, D. A. Weitz, S. Seiffert, *Adv. Healthcare Mater.* **2015**, *4*, 1841; d) M. M. Perera, D. M. Fischesser, J. D. Molkentin, N. Ayres, *Polym. Chem.* **2019**, *10*, 6360.

[7] H. Y. Yoshikawa, F. F. Rossetti, S. Kaufmann, T. Kaindl, J. Madsen, U. Engel, A. L. Lewis, S. P. Armes, M. Tanaka, *J. Am. Chem. Soc.* **2011**, *133*, 1367.

[8] a) B. M. Gillette, J. A. Jensen, M. Wang, J. Tchao, S. K. Sia, *Adv. Mater.* **2010**, *22*, 686; b) F. X. Jiang, B. Yurke, R. S. Schloss, B. L. Firestein, N. A. Langrana, *Biomaterials* **2010**, *31*, 1199; c) D. C. Lin, B. Yurke, N. A. Langrana, *J. Mater. Res.* **2005**, *20*, 1456; d) M. Bril, S. Fredrich, N. A. Kurniawan, *Smart Mater. Med.* **2022**, *3*, 257.

[9] E. D. van Deel, A. Najafi, D. Fontoura, E. Valent, M. Goebel, K. Kardux, I. Falcão-Pires, J. van der Velden, *The J. Phys.* **2017**, *595*, 4597.

[10] K. Suzuki, S. Miyagawa, L. Liu, T. Kawamura, J. Li, X. Qu, A. Harada, K. Toda, D. Yoshioka, S. Kainuma, A. Kawamura, Y. Sawa, *The J. Heart Lung Transplant.* **2021**, *40*, 767.

[11] a) D. Motlagh, T. J. Hartman, T. A. Desai, B. Russell, *J. Biomed. Mater. Res., Part A* **2003**, *67A*, 148; b) L. Ren, X. Zhou, R. Nasiri, J. Fang, X. Jiang, C. Wang, M. Qu, H. Ling, Y. Chen, Y. Xue, M. C. Hartel, P. Tebon, S. Zhang, H. J. Kim, X. Yuan, A. Shamloo, M. R. Dokmeci, S. Li, A. Khademhosseini, S. Ahadian, W. Sun, *Small Methods* **2020**, *4*, 2000438; c) A. Navaei, N. Moore, R. T. Sullivan, D. Truong, R. Q. Migrino, M. Nikkhah, *RSC Adv.* **2017**, *7*, 3302; d) C. J. Bettinger, R. Langer, J. T. Borenstein, *Angew. Chem. Int. Ed. Eng.* **2009**, *48*, 5406; e) M. K. Driscoll, X. Sun, C. Guven, J. T. Fourkas, W. Losert, *ACS Nano* **2014**, *8*, 3546.

[12] a) N. Jiwlawat, E. M. Lynch, B. N. Napiwocki, A. Stempien, R. S. Ashton, T. J. Kamp, W. C. Crone, M. Suzuki, *Biotechnol. Bioeng.* **2019**, *116*, 2377; b) K. M. C. Tsang, N. Annabi, F. Ercole, K. Zhou, D. J. Karst, F. Li, J. M. Haynes, R. A. Evans, H. Thissen, A. Khademhosseini, J. S. Forsythe, *Adv. Funct. Mater.* **2015**, *25*, 977.

[13] E. A. Corbin, A. Vite, E. G. Peyster, M. Bhoopalam, J. Brandimarto, X. Wang, A. I. Bennett, A. T. Clark, X. Cheng, K. T. Turner, K. Musunuru, K. B. Margulies, *ACS Appl. Mater. Interfaces* **2019**, *11*, 20603.

[14] D. Schuftan, Y. K. G. Kooh, J. Guo, Y. Sun, L. Aryan, B. Stottlemire, C. Berkland, G. M. Genin, N. Huebsch, *J. Biomed. Mater. Res. Part A* **2024**, *112*, 534.

[15] Z. Cao, J. K. Ball, A. H. Lateef, C. P. Virgile, E. A. Corbin, *ACS Omega* **2023**, *8*, 5406.

[16] a) X. Bai, *Cells* **2020**, *9*, 2193; b) A. Hasan, N. Mohammadi, A. Nawaz, T. Kodagoda, I. Diakonov, S. E. Harding, *J. Gorelik, Cells* **2020**, *9*, 2275; c) M. Ishida, S. Miyagawa, A. Saito, S. Fukushima, A. Harada, E. Ito, F. Ohashi, T. Watabe, J. Hatazawa, K. Matsuura, Y. Sawa, *Transplantation* **2019**, *103*, 291; d) S. Kussauer, R. David, H. Lemcke, *Cells* **2019**, *8*, 1331; e) Z. Qian, D. Sharma, W. Jia, D. Radke, T. Kamp, F. Zhao, *Theranostics* **2019**, *9*, 2143; f) T. U. Esser, A. Anspach, K. A. Muenzebrock, D. Kah, S. Schrüfer, J. Schenk, K. G. Heinze, D. W. Schubert, B. Fabry, F. B. Engel, *Adv. Mater.* **2023**, *35*, 2305911.

[17] a) Y. Jiang, P. Park, S. M. Hong, K. Ban, *Mol. Cells* **2018**, *41*, 613; b) C. C. Veerman, G. Kosmidis, C. L. Mummery, S. Casini, A. O. Verkerk, M. Bellin, *Stem Cells Dev.* **2015**, *24*, 1035; c) C. Robertson, D. D. Tran, S. C. George, *Stem Cells* **2013**, *31*, 829; d) B. L. Tang, *Cells* **2020**, *9*, 240.

[18] a) T. Crestani, C. Steichen, E. Neri, M. Rodrigues, M. H. Fonseca-Alaniz, B. Ormrod, M. R. Holt, P. Pandey, S. Harding, E. Ehler, J. E. Krieger, *Biochem. Biophys. Res. Commun.* **2020**, *533*, 376; b) M. Carlos-Oliveira, F. Lozano-Juan, P. Occhetta, R. Visone, M. Rasponi, *Biophys. Rev.* **2021**, *13*, 717; c) W. Dou, L. Wang, M. Malhi, H. Liu, Q. Zhao, J. Plakhotnik, Z. Xu, Z. Huang, C. A. Simmons, J. T. Maynes, Y. Sun, *Biosens. Bioelectron.* **2021**, *175*, 112875; d) A. Leonard, A. Bertero, J. D. Powers, K. M. Beussman, S. Bhandari, M. Regnier, C. E. Murry, N. J. Sniadecki, *J. Mol. Cell. Cardiol.* **2018**, *118*, 147.

[19] a) M. Wanjare, L. Hou, K. H. Nakayama, J. J. Kim, N. P. Mezak, O. J. Abilez, E. Tzatzalos, J. C. Wu, N. F. Huang, *Biomater. Sci.* **2017**, *5*, 1567; b) C. A. Werley, M. P. Chien, J. Gaublomme, K. Shekhar, V. Butty, B. A. Yi, J. M. Kralj, B. B. Bloxham, L. A. Boyer, A. Regev, A. E. Cohen, *PloS one* **2017**, *12*, e0172671; c) C. Xu, L. Wang, Y. Yu, F. Yin, X. Zhang, L. Jiang, J. Qin, *Biomater. Sci.* **2017**, *5*, 1810; d) I. Batalov, Q. Jallerat, S. Kim, J. Bliley, A. W. Feinberg, *Sci. Rep.* **2021**, *11*, 11502.

[20] A. Körner, M. Mosqueira, M. Hecker, N. D. Ullrich, *Front. Physiol.* **2021**, *12*, 710619.

[21] S. Yoshida, S. Miyagawa, S. Fukushima, T. Kawamura, N. Kashiyama, F. Ohashi, T. Toyofuku, K. Toda, Y. Sawa, *Mol. Ther.* **2018**, *26*, 2681.

[22] N. Kumar, J. A. Dougherty, H. R. Manring, I. Elmadbouh, M. Mergaye, A. Czirok, D. G. Isai, A. E. Belevych, L. Yu, P. M. L. Janssen, P. Fadda, S. Gyorke, M. A. Ackermann, M. G. Angelos, M. Khan, *Sci. Rep.* **2019**, *9*, 13188.

[23] a) M. Ouyang, R. J. Muisener, A. Boulares, J. T. Koberstein, *J. Membr. Sci.* **2000**, *177*, 177; b) K. Efimenko, W. E. Wallace, J. Genzer, *J. Colloid Interface Sci.* **2002**, *254*, 306.

[24] a) J. Y. Chung, A. J. Nolte, C. M. Stafford, *Adv. Mater.* **2011**, *23*, 349; b) K. Efimenko, M. Rackaitis, E. Manias, A. Vaziri, L. Mahadevan, J. Genzer, *Nat. Mater.* **2005**, *4*, 293.
[25] C. M. Stafford, C. Harrison, K. L. Beers, A. Karim, E. J. Amis, M. R. VanLandingham, H. C. Kim, W. Volksen, R. D. Miller, E. E. Simonyi, *Nat. Mater.* **2004**, *3*, 545.
[26] A. House, J. Cornick, Q. Butt, M. Guvendiren, *J. Biomed. Mater. Res., Part A* **2023**, *111*, 1228.
[27] A. Buxboim, K. Rajagopal, A. E. Brown, D. E. Discher, *J. Phys. Condens. Matter* **2010**, *22*, 194116.
[28] M. F. Berry, A. J. Engler, Y. J. Woo, T. J. Pirolli, L. T. Bish, V. Jayasankar, K. J. Morine, T. J. Gardner, D. E. Discher, H. L. Sweeney, *Am. J. Physiol.: Heart Circ. Physiol.* **2006**, *290*, H2196.
[29] W. Wan, K. K. Bjorkman, E. S. Choi, A. L. Panepento, K. S. Anseth, L. A. Leinwand, *Biorxiv* **2019**, 682930, https://doi.org/10.1101/682930.
[30] a) J. G. Jacot, A. D. McCulloch, J. H. Omens, *Biophys. J.* **2008**, *95*, 3479; b) S. Querceto, R. Santoro, A. Gowran, B. Grandinetti, G. Pompilio, M. Regnier, C. Tesi, C. Poggesi, C. Ferrantini, J. M. Pioner, *J. Mol. Cell. Cardiol.* **2022**, *166*, 36.
[31] a) G. Forte, S. Pagliari, M. Ebara, K. Uto, J. K. Tam, S. Romanazzo, C. Escobedo-Lucea, E. Romano, P. Di Nardo, E. Traversa, T. Aoyagi, *Tissue Eng. Part A* **2012**, *18*, 1837; b) M. Tallawi, R. Rai, A. R. Boccaccini, K. E. Aifantis, *Tissue Eng. Part B Rev.* **2015**, *21*, 157; c) M. Johansson, B. Ulfenborg, C. X. Andersson, S. Heydarkhan-Hagvall, A. Jeppsson, P. Sartipy, J. Synnergren, *Biol. Open* **2020**, *9*, bio052381.
[32] P. Bajaj, X. Tang, T. A. Saif, R. Bashir, *J. Biomed. Mater. Res. A* **2010**, *95*, 1261.
[33] N. Gavara, R. S. Chadwick, *Biomech. Model. Mechanobiol* **2016**, *15*, 511.
[34] a) J. Han, Q. Wu, Y. Xia, M. B. Wagner, C. Xu, *Stem Cell Res.* **2016**, *16*, 740; b) M. Khan, Y. Xu, S. Hua, J. Johnson, A. Belevych, P. M. Janssen, S. Gyorke, J. Guan, M. G. Angelos, *PLoS One* **2015**, *10*, e0126338.
[35] a) M. A. Bray, S. P. Sheehy, K. K. Parker, *Cell Motil. Cytoskeleton* **2008**, *65*, 641; b) A. W. Feinberg, P. W. Alford, H. Jin, C. M. Ripplinger, A. A. Werdich, S. P. Sheehy, A. Grosberg, K. K. Parker, *Biomaterials* **2012**, *33*, 5732.
[36] J. G. Jacot, J. C. Martin, D. L. Hunt, *J. Biomech.* **2010**, *43*, 93.
[37] A. G. Rodriguez, S. J. Han, M. Regnier, N. J. Sniadecki, *Biophys. J.* **2011**, *101*, 2455.
[38] K. Roshanbinfar, Z. Mohammadi, A. Sheikh-Mahdi Mesgar, M. M. Dehghan, O. P. Oommen, J. Hilborn, F. B. Engel, *Biomater. Sci.* **2019**, *7*, 3906.
[39] J. Z. Zhang, N. Belbachir, T. Zhang, Y. Liu, R. Shrestha, J. C. Wu, *Stem Cell Rep.* **2021**, *16*, 168.
[40] P. Wu, G. Deng, X. Sai, H. Guo, H. Huang, P. Zhu, *Biosci. Rep.* **2021**, *41*, BSR20200833.
[41] a) Y. C. Tsan, S. J. DePalma, Y. T. Zhao, A. Capilnasiu, Y. W. Wu, B. Elder, I. Panse, K. Ufford, D. L. Matera, S. Friedline, T. S. O'Leary, N. Wubshet, K. K. Y. Ho, M. J. Previs, D. Nordsletten, L. L. Isom, B. M. Baker, A. P. Liu, A. S. Helms, *Nat. Commun.* **2021**, *12*, 6167; b) J. H. Ahrens, S. G. M. Uzel, M. Skylar-Scott, M. M. Mata, A. Lu, K. T. Kroll, J. A. Lewis, *Adv. Mater.* **2022**, *34*, 2200217; c) A. J. Engler, C. Carag-Krieger, C. P. Johnson, M. Raab, H.-Y. Tang, D. W. Speicher, J. W. Sanger, J. M. Sanger, D. E. Discher, *J. Cell Sci.* **2008**, *121*, 3794.
[42] a) N. Hersch, B. Wolters, G. Dreissen, R. Springer, N. Kirchgeßner, R. Merkel, B. Hoffmann, *Biol. Open* **2013**, *2*, 351; b) J. L. Young, A. J. Engler, *Biomaterials* **2011**, *32*, 1002.
[43] S. Khetan, M. Guvendiren, W. R. Legant, D. M. Cohen, C. S. Chen, J. A. Burdick, *Nat. Mater.* **2013**, *12*, 458.
[44] M. Guvendiren, S. Yang, J. A. Burdick, *Adv. Funct. Mater.* **2009**, *19*, 3038.
[45] M. Ibrahim, P. Kukadia, U. Siedlecka, J. E. Cartledge, M. Navaratnarajah, S. Tokar, C. Van Doorn, V. T. Tsang, J. Gorelik, M. H. Yacoub, C. M. Terracciano, *J. Cell. Mol. Med.* **2012**, *16*, 2910.